Biosensors and Bioelectronics 102 (2018) 247–255

Contents lists available at ScienceDirect

Biosensors and Bioelectronics

journal homepage: www.elsevier.com/locate/bios

# Effect of Brownian motion on reduced agglomeration of nanostructured metal oxide towards development of efficient cancer biosensor

Suveen Kumar[a], Ashish[b], Saurabh Kumar[a], Shine Augustine[a], Santosh Yadav[c], Birendra Kumar Yadav[d], Rishi Pal Chauhan[b], Ajay Kumar Dewan[d], Bansi Dhar Malhotra[a,*]

[a] Nanobioelectronics Laboratory, Department of Biotechnology, Delhi Technological University, Delhi 110042, India
[b] School of Biomedical Engineering, National Institute of Technology Kurukshetra, Haryana 136119, India
[c] Institute of Genomics and Integrative Biology, Delhi 110007, India
[d] Rajiv Gandhi Cancer Institute and Research Centre, Delhi 110085, India

ARTICLE INFO

*Keywords:*
Brownian motion
Hafnium oxide
Reduced graphene oxide
Cancer
Biosensor

ABSTRACT

We report results of the studies relating to fabrication of nanostructured metal oxide (NMO) based cancer biosensor. With the help of 2D electroactive reduced graphene oxide (RGO), we successfully inhibited the Brownian motion of NMO that led to reduced agglomeration of NMO. The nanostructured hafnium oxide ($nHfO_2$) was used as a model NMO. The reduced agglomeration of $nHfO_2$ was achieved through controlled hydrothermal synthesis and investigated via nanoparticles tracking analysis (NTA). X-ray diffraction (XRD), scanning electron microscopy (SEM) and transmission electron microscope (TEM) techniques were used for phase identification as well as morphological analysis of the synthesized nanohybrid ($nHfO_2$@RGO) material. The 3-aminopropyl triethoxysilane (APTES) was used for the functionalization of $nHfO_2$@RGO and electrophoretic deposition (EPD) technique was used for its deposition onto ITO coated glass electrode. Further, antibodies of cancer biomarker (anti-CYFRA-21-1) were immobilized via EDC-NHS chemistry and Bovine serum albumin (BSA) was used for blocking of the non-specific binding sites. The electrochemical response studies of fabricated immunoelectrode (BSA/anti-CYFRA-21-1/APTES/$nHfO_2$@RGO/ITO) revealed higher sensitivity (18.24 μA mL $ng^{-1}$), wide linear detection range (0 to 30 ng $mL^{-1}$), with remarkable lower detection limit (0.16 ng $mL^{-1}$). The obtained results showed good agreement with the concentration of CYFRA-21-1 obtained through enzyme linked immunosorbent assay (ELISA) in saliva samples of oral cancer patients.

## 1. Introduction

Nanostructured metal oxides (NMOs) owing to their unique physical, chemical and electronic properties have recently drawn much interest towards the fabrication of various biosensing platforms (Luo et al., 2006; Solanki et al., 2011). These materials provide high surface-to-volume ratio, surface reaction activity, chemical, thermal and mechanical stability, high catalytic efficiency as well as strong adsorption ability that can facilitate immobilization of biomolecules with desired orientation (Malhotra et al., 2012; Solanki et al., 2009). A number of metal oxides including zinc oxide, iron oxide, titanium oxide, zirconium oxide, magnesium oxide, hafnium oxide etc. have been used for application in biosensors (Das et al., 2011; Kumar et al., 2016c; Lee et al., 2012; Malhotra et al., 2012; Solanki et al., 2011). Among the various metal oxides, nanostructured hafnium oxide ($nHfO_2$) has recently aroused considerable interest for the fabrication of biosensing platforms. This NMO exhibits high dielectric constant (20 − 25), large surface-to-volume ratio, thermal stability, non-toxicity, pH sensitivity with neutral isoelectric point (7.0) and is thus a promising candidate for fabrication of desired biosensing platform (Chen et al., 2010; Fahrenkopf et al., 2012; Lee et al., 2012). Further, the presence of oxygen moieties in $nHfO_2$ facilitates covalent conjugation of linker molecules (APTES) with hydrolyzed ITO electrode (Fahrenkopf et al., 2012; Shim et al., 2013). It has been predicted that Brownian motion of the suspended dispersed $nHfO_2$ in solution may result in agglomeration resulting in the formation of large cluster molecules with low surface-to-volume ratio that may influence the biosensing parameters.(Eliziário et al., 2009; Lee et al., 2006) However, this problem may perhaps be overcome by inhibiting Brownian motion in $nHfO_2$ by providing supporting matrix that has high surface area, large number of electroactive sites with conducting behavior.

The chemically reduced graphene oxide is an organic material and is a promising substrate for uniform distribution of NMOs due to its rich defects and electroactive sites that may prevent the agglomeration of

* Corresponding author.
*E-mail address:* bansi.malhotra@gmail.com (B.D. Malhotra).

https://doi.org/10.1016/j.bios.2017.11.004
Received 17 August 2017; Received in revised form 13 October 2017; Accepted 1 November 2017
Available online 10 November 2017
0956-5663/ 

nanosized molecules. Besides this, the reduced chemical groups may facilitate charge transfer kinetics leading to enhanced electrochemical properties that may provide both covalent and non-covalent sites for surface functionalization resulting in improved biomolecules loading with uniform conducting surface (Ali et al., 2016; Ibrahim et al., 2016; Teymourian et al., 2014; Yang et al., 2016).

RGO is known to have excellent electrochemical conductivity, rapid heterogeneous electron transfer rate (HET), superior mechanical flexibility and remarkable stability that may assist the fabrication of efficient biosensing platform (Ali et al., 2016; Teymourian et al., 2014; Yang et al., 2016). Integration of RGO with NMOs may produce synergistic effect resulting in enhanced conductivity, stability, better catalytic behavior and improved charge transfer kinetics (Teymourian et al., 2014; Xu et al., 2013). It has been found that RGO incorporated NMOs can provide a stable nanohybrid through mutual electrostatic interactions between the positively charged NMOs and negatively charged RGO sheet preventing agglomeration of NMOs onto RGO sheet resulting in improved electrochemical properties (Ali et al., 2016). Teymourian et al. fabricated electrochemical biosensors based on nanocomposite of zirconia decorated reduced graphene oxide wherein improved electrochemical performance was found for different electroactive compounds (Teymourian et al., 2013). Yang et al. demonstrated RGO/$Fe_3O_4$/CdSe nanocomposite based chemiluminescence immunosensor for interleukin-6 detection. Xie et al. reported $CO_3O_4$-RGO nanocomposite based biosensor for glucose detection that showed wide linear range (Xie et al., 2013).

Oral cancer (OC) has become the 6th most common cancer in the world and is known to occur more often in men than women. The OC if not detected at an early stage, may metastasize to other parts of body leading to death. Conventional techniques such as brush cytological tests, laser capture microdissection, biopsy and toluidine blue staining are currently being used for diagnosis of oral cancer (Kumar et al., 2015). However, these methods are invasive and highly painful as they require tissue sample. Moreover, these methods are labor intensive, expensive, time consuming and require skilled personnel for specimen collection and analysis. Thus, demand for a non-invasive biosensing technique for rapid and early detection of OC is increasing. In this context, saliva has been used as an efficient biological medium for its detection. Biologically it is similar to blood sample because level of biomolecules changes with the progression of disease (Kumar et al., 2015).

Saliva has various advantages over blood such as collection is non-invasive, painless sample collection, easy handling and for storage it does not require anticoagulant (de Almeida et al., 2008; Giannobile et al., 2009; Kumar et al., 2016c). In saliva sample of OC patients several biomolecules such as sialic acid, CD-59, TNF-α, CA-125, miR-125a, miR-200a, IL-1, IL-6, IL-8 etc. are secreted in low concentration (Cheng et al., 2014; Hu et al., 2008; Kumar et al., 2013; Lee and Wong, 2009; Markopoulos et al., 2010; Park et al., 2009). Recently for non-invasive detection of OC, CYFRA-21-1 biomarker has been found to play an important role due to its higher secretion as well as a specific cut off value (Malhotra et al., 2016; Rajkumar et al., 2015). Efforts have been made to detect CYFRA-21-1 biomarker in saliva. Kumar et al. reported electrochemical biosensors based on $nZrO_2$ and its composite, $nHfO_2$ for oral cancer biomarker detection. These biosensors were found to have inferior biosensing parameters (Kumar et al., 2016a, 2015, 2016b, 2016c; Tiwari et al., 2016). To overcome these limitations, reduced the agglomeration of NMO by controlling its Brownian motion, may perhaps play an important role.

We report for the first time the facile one pot *in situ* synthesis of $nHfO_2$@RGO nanohybrid towards reduced agglomeration of $nHfO_2$ and its application in development of cancer biosensor. As compared to that based on agglomerated $nHfO_2$, the synthesized non-agglomerated $nHfO_2$ onto RGO based immunosensor exhibited eleven times more HET rate and have superior biosensing parameters.

## 2. Experimental section

### 2.1. Fabrication of immunosensing platform

To fabricate BSA/anti-CYFRA-21-1/APTES/$nHfO_2$@RGO/ITO immunoelectrode, the functionalized $nHfO_2$@RGO nanohybrid (APTES/$nHfO_2$@RGO) was deposited onto a pre-hydrolyzed indium tin oxide (ITO) coated glass substrate via EPD technique. The ITO was used as the working electrode, platinum wire as a reference electrode. Both electrodes were separated by 1 cm in the glass cell. Further, 25 mg of APTES/$nHfO_2$@RGO was dispersed in 25 mL of acetonitrile to form the colloidal suspension. An optimized DC potential (35 V) was applied for 60 s to obtain uniform film of APTES/$nHfO_2$@RGO onto ITO electrode. Next, a solution containing 15 μL of anti-CYFRA-21-1 (50 μg $mL^{-1}$), 7.5 μL of EDC (0.2 M) and 7.5 μL of NHS (0.05 M) was prepared, where EDC acted as coupling agent and NHS for the activation of -COOH group present on anti-CYFRA-21-1 molecules. 30 μL of activated anti-CYFRA-21-1 (50 μg $mL^{-1}$) solution was drop cast over APTES/$nHfO_2$@RGO/ITO electrode and was kept in a humid chamber for about 3 h. After incubation the electrode was washed with PBS solution (pH = 7.0) to remove any unbound antibody molecules. Further, for blocking of the non-specific active sites, 30 μL of freshly prepared BSA (1 mg $mL^{-1}$) was used. The fabricated BSA/anti-CYFRA-21-1/APTES/$nHfO_2$@RGO/ITO immunoelectrode was further washed with PBS solution and stored at 4 °C till further use. Scheme S1 shows the schematic representation of immunoelectrode fabrication.

## 3. Results and discussion

### 3.1. Structural and morphological studies

Fig. 1a shows the XRD pattern of synthesized $nHfO_2$@RGO nanohybrid in the 2θ range 20° to 80°. The peak at 24.4° corresponding to (002) plane reveals the conversion of GO to RGO through hydrothermal process.(Srivastava et al., 2013) The other peaks obtained at 2θ angle of 28.5°, 31.6°, 34.7°, 38.9°, 41.1°, 45.3°, 50.3°, 55.7°, 61.7°, 65.8°, 71.4°, 75.6° and 77.9° correspond to (−111), (111), (020), (021), (−112), (211), (022), (310), (311), (−231), (123), (140) and (330) planes, respectively indicating the formation of monoclinic phase of $nHfO_2$ (JCPDS No. 340104). No additional peak was observed indicating the synthesis of pure monoclinic phase of $nHfO_2$ with RGO sheet. The crystalline size of hafnium oxide was calculated as 10 nm for the (020) plane using Scherrer formula (Eq. (1)) indicating the presence of hafnium oxide crystallites grown along the (020) direction.

$$D = \frac{0.94\lambda}{\beta Cos\theta} \quad (1)$$

where D is the crystalline size of the nanomaterial, λ is the X-ray wavelength (1.540 Å), β is the full width at half maxima and θ is the Bragg's angle.

The size of synthesized nanoparticles plays an important role in the efficiency of the biosensing parameters. Kumar et al. (2016b) synthesized $nHfO_2$ nanoparticles via hydrothermal process. During this, the nanoparticles undergo Brownian motion due to their random collision leading to the agglomeration and formation of larger particles (~120 nm) whereas; the individual size of the synthesized $nHfO_2$ was ~14 nm (Fig. S1). Brownian motion of the particle is known to be directly proportional to the diffusion coefficient (D) of the particle which can be calculated by the Stoke Einstein equation (Eq. (2)):

$$D = \frac{K_B T}{6\pi\eta r} \quad (2)$$

where $K_B$ is Boltzmann constant ($1.38 \times 10^{-23}$ J/K), T is temperature, η is dynamic viscosity of the solvent and r is hydrodynamic radius of the particle. The diffusion coefficient of $nHfO_2$ (individual particle size of $nHfO_2$ = 14 nm) was calculated to be $1.75 \times 10^{-9}$ $m^2/s$ due to the

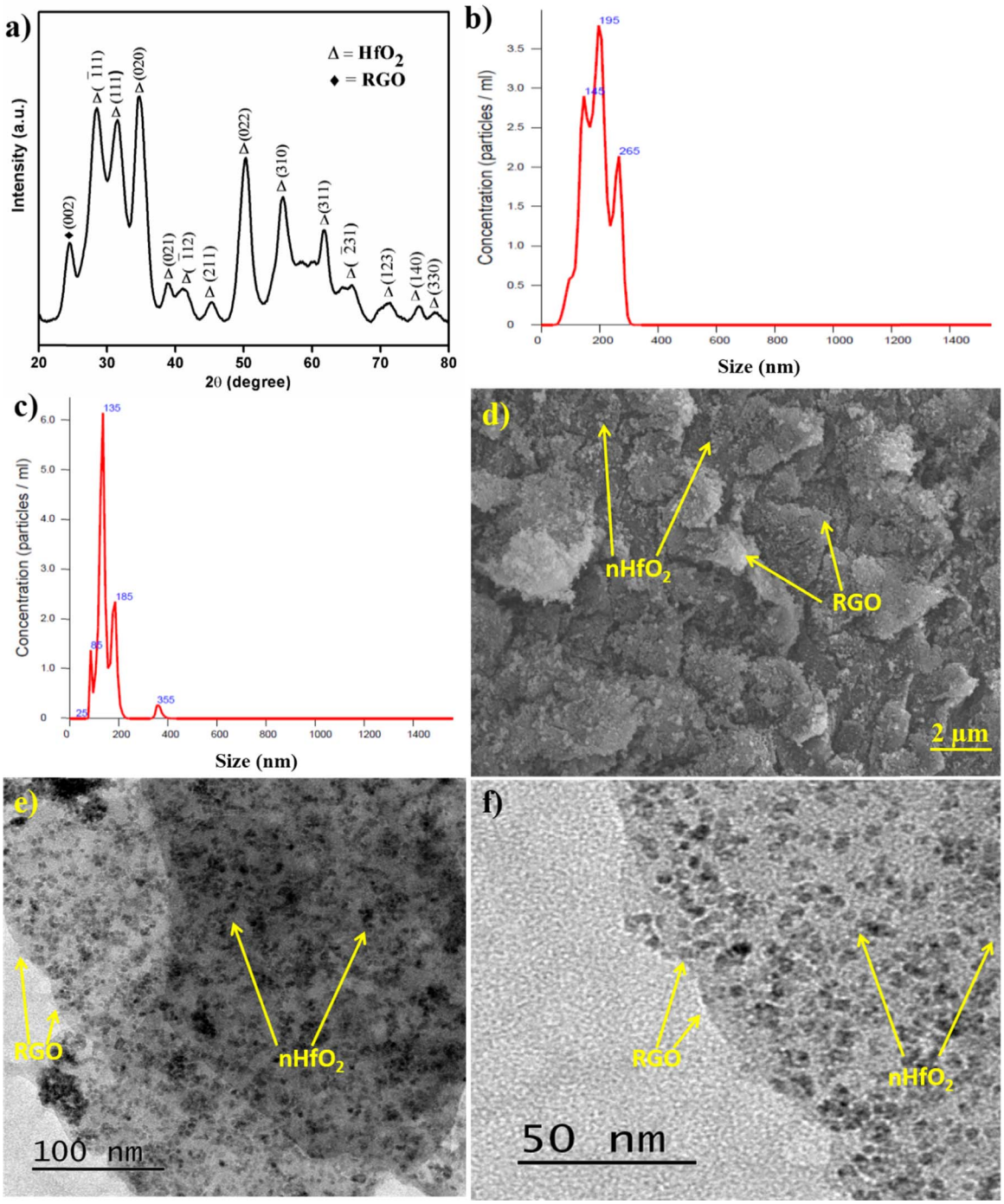


**Fig. 1. (a)** XRD spectra $nHfO_2$@RGO nanohybrid, particle size distribution of **(b)** $nHfO_2$ **(c)** $nHfO_2$@RGO in aqueous solution measured using Nanoparticle Tracking Analysis (NTA) **(d)** SEM image and **(e-f)** TEM images of $nHfO_2$@RGO nanohybrid.

absence of supporting substrate, $nHfO_2$ resulting in agglomeration. This agglomeration of $nHfO_2$ was further investigated by NTA where mean size of hafnia nanoparticles in aqueous solution was found to be ~190 nm (Fig. 1b).

Agglomeration can perhaps be avoided by using a supporting substrate bearing opposite charge that may help in easier binding of the desired nanoparticles to the supporting substrate. In addition to this, the presence of defects on the surface of supporting substrate may further prevent agglomeration of the nanoparticles. In the present work, RGO was used as a supporting substrate that had high conductivity resulting in enhanced biosensing parameters. It may be noted that the particles with higher Brownian motion may result in increased value of diffusion coefficient leading to uniform distribution of the nanomaterial ($nHfO_2$@RGO) onto the substrate. The diffusion coefficient of $nHfO_2$@RGO (individual particle size of $nHfO_2 = 10$ nm) was calculated to be $2.45 \times 10^{-9}$ $m^2/s$ indicating that $nHfO_2$@RGO was 1.4 times more diffusive compared to that of $nHfO_2$ ($1.75 \times 10^{-9}$ $m^2/s$). It appeared that the cumulative properties of the synthesized nanohybrid (i.e. defects and negative zeta potential of RGO and positive zeta potential of $nHfO_2$) perhaps led to reduced agglomeration and uniform decoration. Fig. 1c shows the size distribution of $nHfO_2$@RGO nanohybrid measured in aqueous solution using NTA. The mean size was found to be ~147 nm corresponding to the RGO sheets decorated with $nHfO_2$ nanoparticles. The overall reduction in size of this nanohybrid in

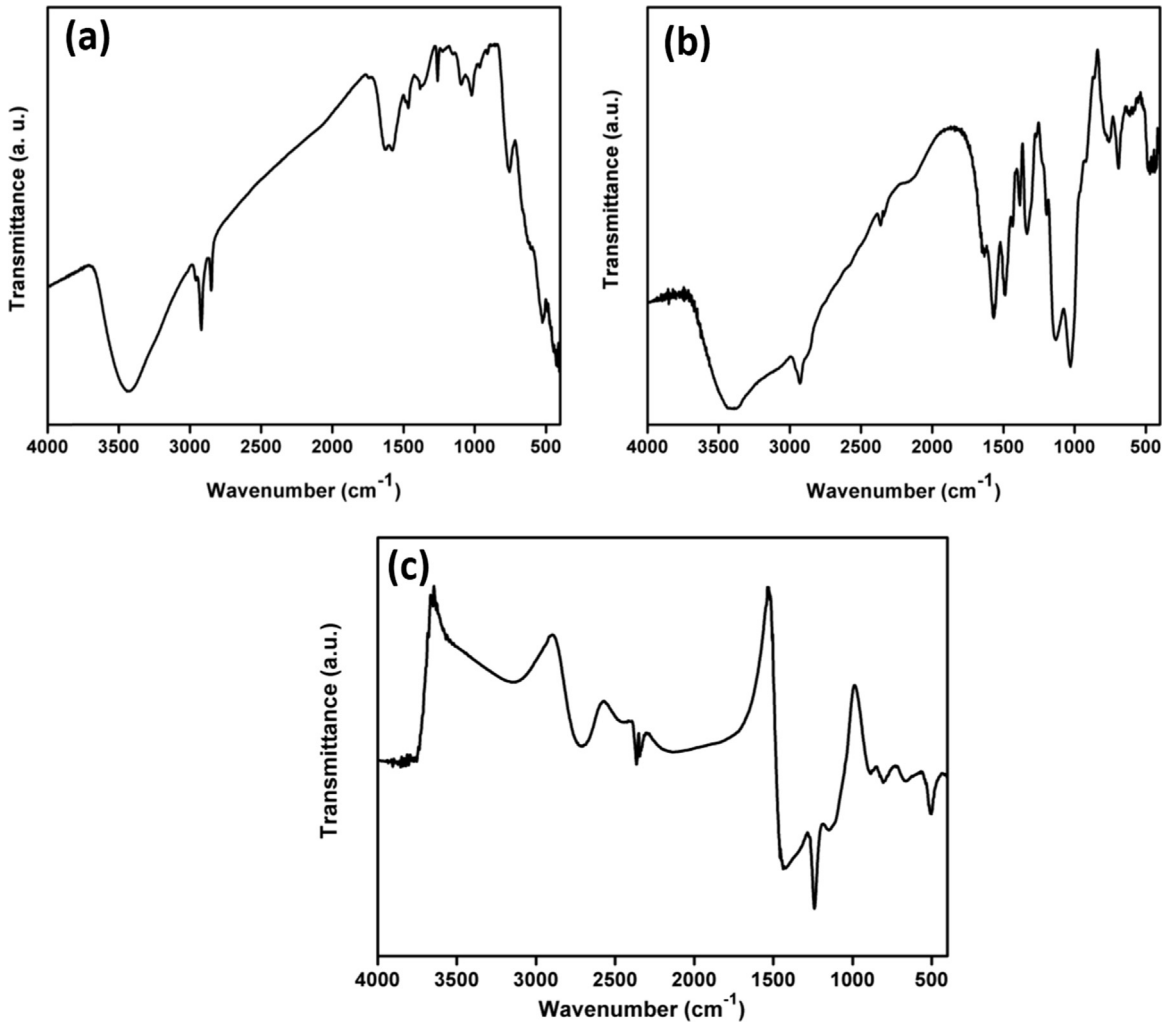


**Fig. 2.** FT-IR spectra of (a) $nHfO_2$@RGO, (b) APTES/$nHfO_2$@RGO and (c) anti-CYFRA-21-1/APTES/$nHfO_2$@RGO/ITO electrode.

comparison to $nHfO_2$ may be attributed to reduced agglomeration and uniform distribution of nanohybrid (Fig. S2). The decoration of $nHfO_2$ onto the RGO surface has been morphologically confirmed through scanning electron microscopy as well as transmission electron microscopy.

The SEM image of $nHfO_2$@RGO nanohybrid (Fig. 1d) indicated uniform deposition of $nHfO_2$ onto the RGO sheet. Fig. 1e-f shows the TEM images of $nHfO_2$@RGO nanohybrid at different magnifications. These results revealed the synthesis of uniformly imbedded nanostructured hafnia onto RGO sheet. The average size of hafnia (10 nm) with spherical outline revealed its nanostructured morphology.

### 3.2. Fourier Transform infrared (FT-IR) spectroscopy

Fig. 2a, b and c show the FT-IR spectra of $nHfO_2$@RGO, APTES/$nHfO_2$@RGO and anti-CYFRA-21-1/APTES/$nHfO_2$@RGO/ITO electrode, respectively. In all three spectra, bands obtained at 520 and in between 1000 and 1300 $cm^{-1}$ indicated the presence of Hf=O bond present in $nHfO_2$ molecules (Pavia et al., 2008) and C-O bond of carboxylic acid onto RGO sheet respectively. Further, bands observed at 2845, 2920 and in the range of 3100–3670 $cm^{-1}$ correspond to -OH group of carboxylic acid present on RGO sheet (Pavia et al., 2008). These results confirmed the presence of both RGO and hafnia molecules. Fig. 2b shows the FT-IR spectra obtained for the functionalized $nHfO_2$@RGO nanohybrid with APTES molecules. The bands obtained at 1490, 1570 and 1649 $cm^{-1}$ indicated bending of $–CH_2$ molecules present in APTES molecules. Bands seen at 2365, 2925 and in between 3075 and 3700 $cm^{-1}$ were due to the combined effect of -OH present on RGO and primary amine (N-H) of APTES molecule and indicated the functionalization of $nHfO_2$@RGO with APTES molecules. The FT-IR spectra of anti-CYFRA-21-1/APTES/$nHfO_2$@RGO/ITO immunoelectrode exhibited an addition band at 1240 $cm^{-1}$ (Fig. 2c) indicating the presence of C-N bond between carboxylic acid (-COOH) of the Fc region of anti-CYFRA-21-1 and -$NH_2$ group at the APTES/$nHfO_2$@RGO/ITO electrode revealing successful immobilization of anti-CYFRA-21-1 onto APTES/$nHfO_2$@RGO/ITO electrode (Pavia et al., 2008).

### 3.3. Electrochemical characterization

DPV and CV studies were conducted to investigate the electrochemical properties of $nHfO_2$@RGO based electrode. Fig. 3a shows results of the pH studies conducted on the BSA/anti-CYFRA21-1/APTES/$nHfO_2$@RGO/ITO immunoelectrode. It was observed that the maximum peak current was obtained at neutral pH. However in acidic or basic medium, the peak current decreased. Decrease in the peak current could be attributed to the fact that the biomolecules were present in their natural form at neutral pH. On the other hand, the bioactivity of biomolecules tended to diminish in acidic as well as alkaline medium due to presence of $H^+$ and $OH^-$ ions. For further electrochemical studies PBS buffer (0.05 M, containing 5 mM $[Fe(CN)_6]^{3-/4-}$) of pH 7.0 was used.

To investigate the HET rate ($k^\circ$) of APTES/$nHfO_2$/ITO and APTES/$nHfO_2$@RGO/ITO electrodes, electrochemical impedance spectroscopy (EIS) was performed at 10 mV in PBS solution (Fig. 3b) and calculated by using Eq. (3).

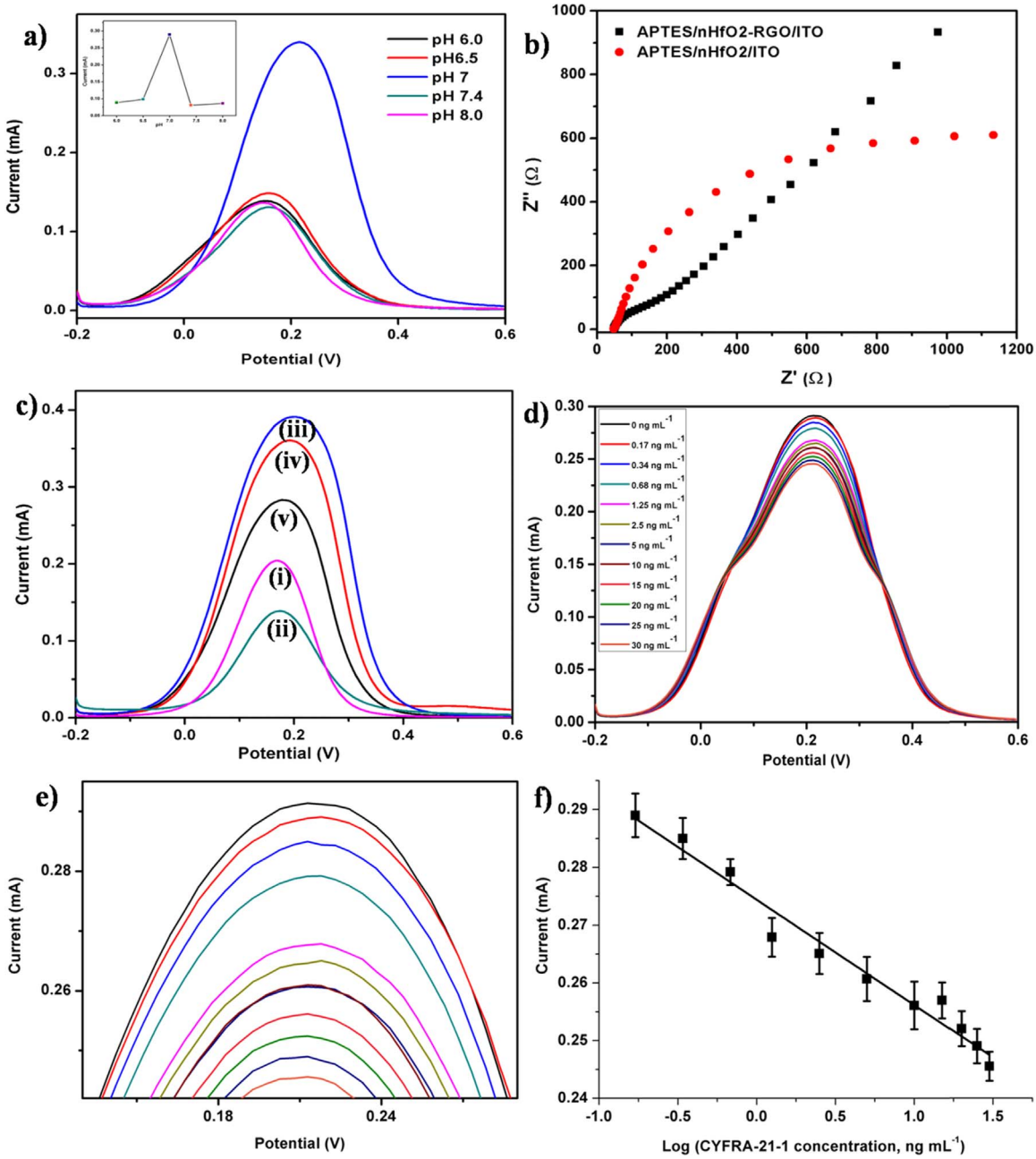


**Fig. 3.** (a) pH response of BSA/anti-CYFRA-21-1/APTES/nHfO$_2$@RGO/ITO immunoelectrode, (b) Electrochemical impedance spectra (EIS) of APTES/nHfO$_2$/ITO and APTES/nHfO$_2$@RGO/ITO electrodes, (c) Electrode studies of (i) ITO (ii) APTES/nHfO$_2$/ITO (iii) APTES/nHfO$_2$@RGO/ITO (iv) anti-CYFRA-21-1/APTES/nHfO$_2$@RGO/ITO (v) BSA/anti-CYFRA-21-1/APTES/nHfO$_2$@RGO/ITO electrodes via DPV technique, (d) Electrochemical response studies of BSA/anti-CYFRA-21-1/APTES/nHfO$_2$@RGO/ITO immunoelectrode as a function of CYFRA-21-1 concentration (0–30 ng mL$^{-1}$) (e) magnified view of oxidation peak current (f) calibration curve between peak current magnitude and CYFRA-21-1 concentration.

$$R_{ct} = \frac{RT}{n^2F^2\,Ak^{\circ}C} \quad (3)$$

where, R is the molar gas constant, T is temperature, n is the number of electrons (n = 1), F is the Faraday constant, A is the active surface area of the electrode, C is the concentration of the electroactive species and $R_{ct}$ is charge transfer resistance of electrode surface. The k° of the APTES/nHfO$_2$@RGO/ITO electrode ($20.28\times10^{-7}$ cm s$^{-1}$) was found to be eleven times higher than that of the APTES/nHfO$_2$/ITO electrode ($1.75\times10^{-7}$ cm s$^{-1}$). This may be due to reduced agglomeration of the nanoparticles and exceptional electrocatalytic properties of RGO, which perhaps provided smooth conduction pathways for charge transfer. (Kumar et al., 2016c; Shin and Hong, 2014)

Fig. 3c shows results of the DPV studies conducted on bare ITO, APTES/nHfO$_2$/ITO, APTES/nHfO$_2$@RGO/ITO, anti-CYFRA-21-1/APTES/nHfO$_2$@RGO/ITO and BSA/anti-CYFRA-21-1/APTES/nHfO$_2$@RGO/ITO electrodes in a potential range from −0.2 to 0.6 V in PBS solution. The magnitude of peak current for APTES/nHfO$_2$/ITO (0.139 mA) electrode was found to be lower than that of bare ITO electrode (0.204 mA). However, magnitude of peak current was found to be increased (0.391 mA) after grafting of nHfO$_2$ with the reduced graphene oxide (RGO). This increase in current could perhaps be due to excellent electrochemical properties of RGO sheet which enabled faster electron transfer kinetics from medium to electrode resulting in increased current. After immobilization of anti-CYFRA-21-1 antibodies onto APTES/nHfO$_2$@RGO/ITO electrode, the magnitude of peak current was found to be 0.361 mA. This decrease in peak current could perhaps be attributed to the insulating nature of antibodies wherein redox active sites were entrapped into macromolecular structure of antibodies.(Ali et al., 2016; Srivastava et al.,

2013) After BSA immobilization, the peak current deceased to 0.283 mA due to blocking of non-specific binding sites of immunoelectrode.(Ali et al., 2016; Kumar et al., 2016c; Srivastava et al., 2013)

To investigate the electrochemical properties of APTES/$nHfO_2$@RGO/ITO and BSA/anti-CYFRA-21-1/APTES/$nHfO_2$@RGO/ITO immunoelectrode, scan rate studies were performed between 50 to 150 mV $s^{-1}$ (Figs. S7 and S8). Inset (i) of Figs. S7 and S8 shows plot between cathodic ($I_{pc}$) and anodic ($I_{pa}$) peak current versus square root of scan rate obtained for APTES/$nHfO_2$@RGO/ITO and BSA/anti-CYFRA-21-1/APTES/$nHfO_2$@RGO/ITO electrodes, respectively. With increasing scan rate, the magnitude of oxidation and reduction peak current shifted towards more positive and negative potential respectively. Besides this, the redox peak current ($I_{pa}$ and $I_{pc}$) varied linearly with square root of scan rate indicating diffusion-controlled process of electrode and can be described by the following Eqs. (4)–(7) (Kumar et al., 2016c; Vasudev et al., 2013).

$$I_1 = [0.196\text{mA(s/mV)} \times (\text{scan rate(mV/s)})^{\frac{1}{2}}] + 0.328\text{mA},\ R^2 = 0.999,\ SD = 1.936 \times 10^{-6} \quad (4)$$

$$I_2 = -[0.169\text{mA(s/mV)} \times \left(\text{scan rate(mV/s)}\right)^{\frac{1}{2}}) - 0.420\text{mA},\ R^2 = 0.997,\ SD = 2.862 \times 10^{-6} \quad (5)$$

$$I_3 = [0.107\text{mA(s/mV)} \times (\text{scan rate(mV/s)})^{\frac{1}{2}}] + 0.177\text{mA},\ R^2 = 0.999,\ SD = 9.978 \times 10^{-7} \quad (6)$$

$$I_4 = -[0.095\text{mA(s/mV)} \times (\text{scan rate(mV/s)})^{\frac{1}{2}}] - 0.204\text{mA},\ R^2 = 0.999,\ SD = 9.965 \times 10^{-7} \quad (7)$$

where $I_1$ and $I_2$ are anodic and cathodic peak current of APTES/$nHfO_2$@RGO/ITO electrode, $I_3$ and $I_4$ are anodic and cathodic peak current of BSA/anti-CYFRA-21-1/APTES/$nHfO_2$@RGO/ITO electrode.

It was found that the difference of cathodic ($E_{pc}$) and anodic ($E_{pa}$) peak potential ($\Delta E_p = E_{pc}$-$E_{pa}$) of APTES/$nHfO_2$@RGO/ITO and BSA/anti-CYFRA-21-1/APTES/$nHfO_2$@RGO/ITO electrodes showed linear relation with square root of scan rate and follow Eqs. (8) and (9). The obtained linear relationship suggests a facile electron transfer from medium to electrode (Inset B in Figs. S7 and S8) indicating that the fabricated electrode is suitable for biosensing platform (Kumar et al., 2016c).

$$\Delta E_p(V)_1 = [0.024V\,(\text{s/mV}) \times (\text{scan rate(mV/s)})^{\frac{1}{2}}] + 0.124\text{V},\ R^2 = 0.999,\ SD = 2.756 \times 10^{-4} \quad (8)$$

$$\Delta E_p(V)_2 = [0.019V\,(\text{s/mV}) \times (\text{scan rate(mV/s)})^{\frac{1}{2}}] + 0.103\text{V},\ R^2 = 0.997,\ SD = 3.158 \times 10^{-4} \quad (9)$$

where $\Delta E_p(V)_1$ and $\Delta E_p(V)_2$ are the difference in cathodic and anodic peak potential of APTES/$nHfO_2$@RGO/ITO and BSA/anti-CYFRA-21-1/APTES/$nHfO_2$@RGO/ITO electrodes, respectively.

The diffusion coefficient (D) of redox species $[Fe(CN)_6]^{3-/4-}$ for the fabricated electrodes was obtained through Randle Sevick equation (Eq. (10)) (Xu et al., 2013).

$$I_p = (2.69\times10^5)n^{3/2}AD^{1/2}C\upsilon^{1/2} \quad (10)$$

where $I_p$ is the peak current of the electrode, n is the number of electrons transferred in the redox reaction (n = 1), A is surface area of the electrode (0.25 $cm^2$), C is the concentration of redox species ($5\times10^{-3}$ mol $cm^{-2}$) and υ is the scanning rate (50 mV $s^{-1}$). The value of "D" was found to be $0.85\times10^{-3}$, $0.76\times10^{-3}$ and $0.62\times10^{-3}$ $cm^2$/s for APTES/$nHfO_2$@RGO/ITO, anti-CYFRA-21-1/APTES/$nHfO_2$@RGO/ITO and BSA/anti-CYFRA-21-1/APTES/$nHfO_2$@RGO/ITO electrodes, respectively. It was found that the BSA/anti-CYFRA-21-1/APTES/$nHfO_2$@RGO/ITO immunoelectrode had lower "D" value ($0.62\times10^{-3}$ $cm^2$/s) with respect to other nanomaterials based immunoelectrodes such as BSA/anti-CYFRA-21-1/$nZrO_2$-RGO/ITO ($1.12\times10^{-3}$ $cm^2$/s) (Kumar et al., 2016c) and BSA/anti-CYFRA-21-1/$nHfO_2$/ITO ($2.12\times10^{-3}$ $cm^2$/s) (Kumar et al., 2016a) indicating that $nHfO_2$@RGO based immunoelectrode is more suitable biosensing platform.

The number of antibodies immobilized onto an immunoelectrode is known to play an important role in fabrication of an efficient biosensing platform. To investigate the number of antibodies molecules covalently immobilized onto BSA/anti-CYFRA-21-1/APTES/$nHfO_2$@RGO/ITO immunoelectrode, Brown-Anson equation (Eq. (11)) was used.

$$I_p = n^2F^2\gamma A\upsilon(4RT)^{-1} \quad (11)$$

where $I_p$ represents the peak current, A is the surface area of the electrode, ν is the scan rate (V/s), γ is the surface concentration of the absorbed electro-active species, F is the Faraday constant, R is the gas constant and T is room temperature. The surface concentration of anti-CYFRA-21-1 onto BSA/anti-CYFRA-21-1/APTES/$nHfO_2$@RGO/ITO immunoelectrode was calculated to be $7.76\times10^{-8}$ mol/$cm^2$ that was higher than the previously reported immunosensing platform i.e. $8.03\times10^{-9}$ mol/$cm^2$ for BSA/anti-CYFRA-21-1/APTES/$nZrO_2$-RGO/ITO (Kumar et al., 2015) and $2.87\times10^{-8}$ mol/$cm^2$ for BSA/anti-CYFRA-21-1/APTES/$nHfO_2$/ITO (Kumar et al., 2016a) immunoelectrode, indicating that $nHfO_2$@RGO possessed increased ability to immobilize more number of biomolecules with respect to previously used nanomaterials.

### 3.4. Detection of salivary oral cancer biomarker

Fig. 3(d) shows the electrochemical response studies of BSA/anti-CYFRA-21-1/APTES/$nHfO_2$@RGO/ITO immunoelectrode conducted as a function of CYFRA-21-1 antigen concentration utilizing DPV technique in PBS solution containing $5\times10^{-3}$ M $[Fe(CN)_6]^{3-/4-}$. The immunoelectrode was incubated for about 15 min prior to measurement for having efficient antigen-antibody interactions. Magnitude of peak current was found to decrease linearly with increasing concentration of CYFRA-21-1 antigen ranging from 0 to 30 ng $mL^{-1}$ (Biosensing parameters based on different size of $nHfO_2$ have been incorporated in the supporting information at Figs. S9, S10 and Table S2) explained by following Eq. (12).

$$I_p = -[(18.24\mu\text{A mL ng}^{-1}) \times (\text{conc. of CYFRA} - 21 - 1(\text{ng mL}^{-1}))] + 0.26\text{mA}, R^2 = 0.96 \quad (12)$$

This decrease in current could be attributed to the formation of electrically insulating immunocomplex arising due to interaction of CYFRA-21-1 antigens with antibodies which acted as a barrier and hindered the transport of generated electrons from medium to electrode.(Ali et al., 2016; Srivastava et al., 2013) The sensitivity of the BSA/anti-CYFRA-21-1/APTES/$nHfO_2$@RGO/ITO immunoelectrode estimated using slope of curve (Fig. 3f) was determined to be 18.24 μA mL $ng^{-1}$ which was more with respect to other similar biosensing platforms (Kumar et al., 2016a, 2015, 2016b, 2016c). Furthermore, the value of lower detection limit (LOD) was estimated to be 0.16 ng $mL^{-1}$ using Eq. (13).

$$\text{LOD} = \frac{3\sigma}{m} \quad (13)$$

where, σ is the standard deviation and m is the slope of the curve.

To investigate the attachment of CYFRA-21-1 onto the immunoelectrode after sensing, we have conducted fluorescence spectroscopy studies (Fig. 4). The obtained fluorescent green colored image indicates the successful binding of the CYFRA-21-1 protein biomarkers onto the immunoelectrode (BSA/anti-CYFRA-21-1/APTES/$nHfO_2$@RGO/ITO) during sensing experiment.

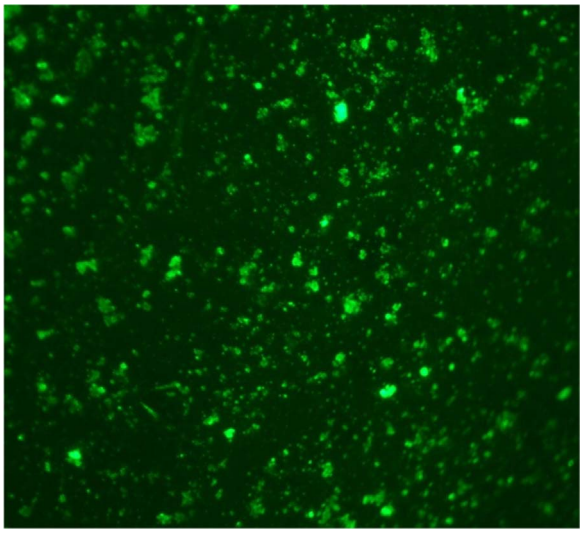

**Fig. 4.** Fluorescence microscopic image of antigen (CYFRA-21-1) bounded BSA/anti-CYFRA-21-1/APTES/nHfO$_2$@RGO/ITO immunoelectrode by using rhodamine 123 dye bounded secondary antibodies.

### 3.5. Control experiment and Interferent studies

A control experiment was performed to determine the electrochemical response of APTES/nHfO$_2$@RGO/ITO electrode with different CYFRA-21-1 antigen concentrations (Fig. 5a). No significant change in the magnitude of peak current was found even at higher concentrations of CYFRA-21-1 antigen. This indicated that CYFRA-21-1 antigens interact specifically with the antibodies present on the surface of BSA/anti-CYFRA-21-1/APTES/nHfO$_2$@RGO/ITO immunoelectrode.

Interferent studies (Fig. 5b) of fabricated BSA/anti-CYFRA-21-1/APTES/nHfO$_2$@RGO/ITO immunoelectrode were performed using DPV by incubating it with different interfering analytes supposed to be present in human saliva such as glucose, $CaCl_2$, $NaHCO_3$, CTn-I, CEA, ET-1, ascorbic acid, lactic acid etc. It was observed that no significant change in magnitude of peak current occurred on addition of different analytes. However, on addition of CYFRA-21-1 antigen magnitude of peak current decreased to 0.25 mA indicating higher selectivity of fabricated BSA/anti-CYFRA-21-1/APTES/nHfO$_2$@RGO/ITO immunoelectrode towards CYFRA-21-1 antigen detection.

### 3.6. Reproducibility and shelf life studies

The reproducibility studies of the fabricated immunoelectrode were conducted by measuring the current response of five different electrodes fabricated under similar conditions (Shown in Fig. 5c). It was observed that all electrodes exhibited about comparable current. Next, the shelf life of fabricated BSA/anti-CYFRA-21-1/APTES/nHfO$_2$@RGO/ITO immunoelectrode was determined by measuring the change in magnitude of peak current at regular 3 days interval for about 40 days and shown in Fig. S11. Immunoelectrode was stored at 4 °C when not in

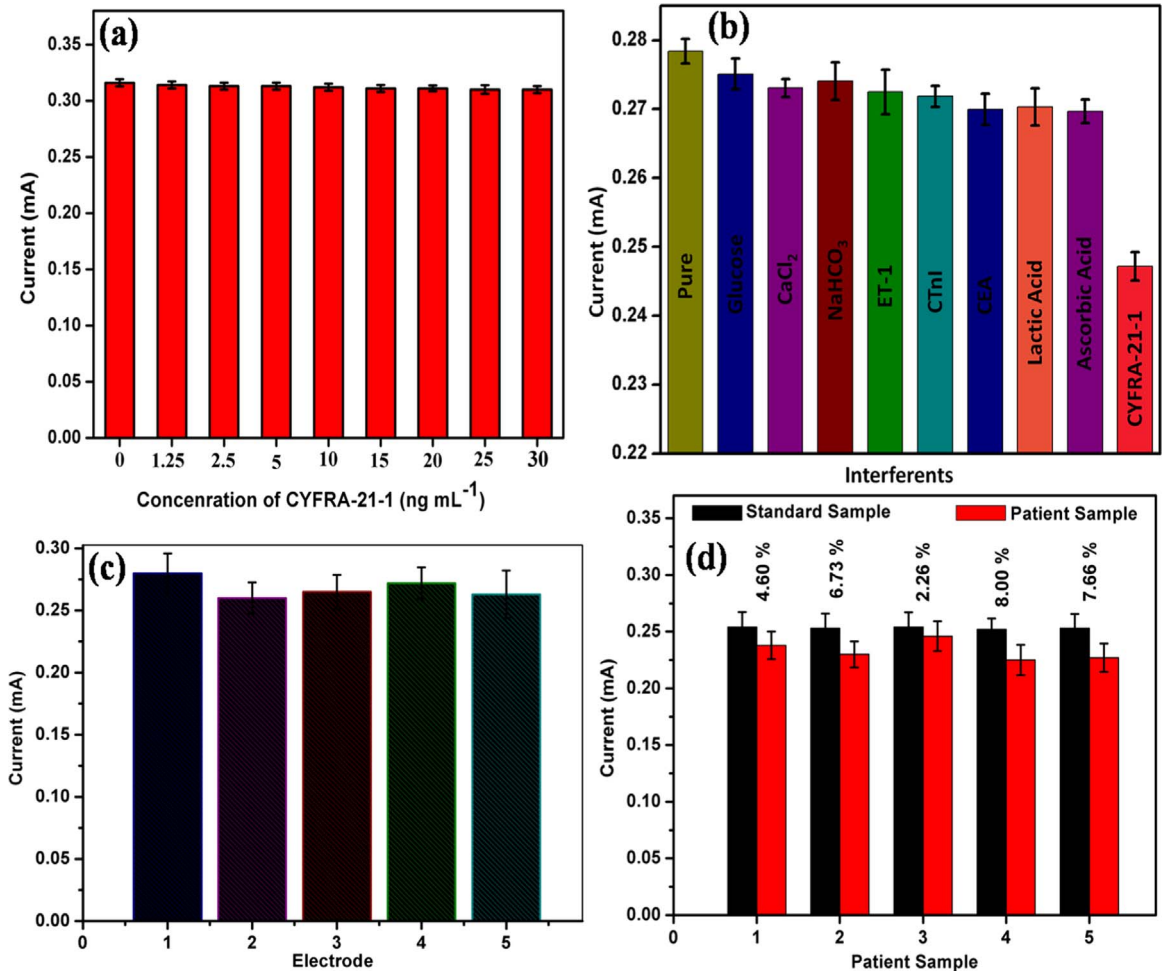


**Fig. 5.** (a) Control studies of APTES/nHfO$_2$@RGO/ITO electrode as a function of CYFRA-21-1 concentration (0–30 ng mL$^{-1}$) (b) Interferent studies of BSA/anti-CYFRA-21-1/APTES/nHfO$_2$@RGO/ITO immunoelectrode, (c) Reproducibility studies and (d) Comparative analysis of current response between standard sample and patient samples using fabricated BSA/anti-CYFRA-21-1/APTES/nHfO$_2$@RGO/ITO immunoelectrode.

**Table 1**
Characteristics of the various biosensors used for oral cancer detection.

| Invasive/Non-invasive | Biomarker | Concentration range of biomarker | Labeled | Detection technique | Materials Used | Linear detection range | Sensitivity | Lower detection limit | Ref. |
|---|---|---|---|---|---|---|---|---|---|
| **Invasive (Serum)** | IL-6 (Protein) | ≤ 6 pg $mL^{-1}$ to ≥ 20 pg $mL^{-1}$ | Yes | Amperometric | Single wall carbon nanotube | 0.5–30 pg $mL^{-1}$ | – | – | Malhotra et al., 2010 |
| | | < 6 pg $mL^{-1}$ to > 20 pg $mL^{-1}$ | | DPV | Graphene oxide/Glassy carbon | 0.002–20 ng $mL^{-1}$ | – | – | Li and Yang, 2011 |
| **Non-invasive (Saliva)** | has-miR-200a (mi-RNA) | – | | CV | Gold | 1 aM-10 fM | – | – | Wang et al., 2013 |
| | CYFRA-21-1 (Protein) | 0–18 ng $mL^{-1}$ | No | CV | APTES/$ZrO_2$/ITO | 2–16 ng $mL^{-1}$ | 2.2 μA mL $ng^{-1}$ | 0.08 ng $mL^{-1}$ | Kumar et al., 2015 |
| | | | | | APTES/n$HfO_2$/ITO | 2–18 ng $mL^{-1}$ | 9.28 μA mL $ng^{-1}$ $cm^{-2}$ | 0.21 ng $mL^{-1}$ | Kumar et al., 2016 |
| | | | | | APTES/n$ZrO_2$-RGO/ITO | 2–22 ng $mL^{-1}$ | 0.756 μA mL $ng^{-1}$ | 0.122 ng $mA^{-1}$ | Kumar et al., 2016 |
| | | | | DPV | Serine/n$ZrO_2$/ITO | 0.01-29 ng $mL^{-1}$ | 0.295 μA mL $ng^{-1}$ | 0.01 ng $mL^{-1}$ | Kumar et al., 2016 |
| | | | | | Cys-La$(OH)_3$/ITO | 0.001-10.2 ng $mL^{-1}$ | 12.044 μA mL $ng^{-1}$ $cm^{-2}$ | 0.001 ng $mL^{-1}$ | Tiwari et al., 2016 |
| | | | | | APTES/n$HfO_2$@RGO/ITO | 0-30 ng $mL^{-1}$ | 18.24 μA mL $ng^{-1}$ | 0.164 ng $mL^{-1}$ | Present Work |

use. The immunoelectrode retained 90% of response for 27 days, after which current decreased to 0.260 mA.

### 3.7. Real sample analysis

A series of CYFRA-21-1 concentrations in saliva samples were obtained by ELISA (Table S3) to validate the electrochemical response of the fabricated biosensor. In brief, anti-CYFRA-21-1 precoated microtiter 96 wells plate have been used in ELISA and follow all the steps as per instruction provided on ELISA kit. After following all the steps, colorimetric reaction occurred and further absorbance was recorded at 450 nm in ELISA plate reader. After obtaining CYFRA-21-1 concentrations, we performed electrochemical analysis. It was observed that a reasonable correlation existed between magnitude of the DPV current response of the fabricated immunoelectrode in the presence of (a) CYFRA-21-1 concentrations in saliva samples determined by ELISA and (b) standard concentration of CYFRA-21-1 (Fig. 5**d**). The observed results exhibited average %RSD (relative standard deviation) to be 5.85, indicating high accuracy of the fabricated biosensor for CYFRA-21-1 biomarker detection. The biosensing characteristics of the proposed immunosensor along with reported in the literature are summarized in the Table 1.

## 4. Conclusions

An efficient and label free immunosensor has been developed for noninvasive detection of oral cancer. The synthesized n$HfO_2$@RGO nanohybrid shows 11 times more HET with respect to agglomerated n$HfO_2$ due to which the developed BSA/anti-CFRA-21-1/APTES/n$HfO_2$/RGO/ITO immunoelectrode shows wider linear detection range 0–30 ng $mL^{-1}$), high sensitivity (18.24 μA mL $ng^{-1}$) and remarkable lower detection limit (0.16 ng $mL^{-1}$). This work opens a new window in development of non-agglomerated nanoparticles by trapping its Brownian motion and helps in fabrication of efficient biosensing platform for infectious, non-infectious, food pathogen and airborne virus detection. Efforts should be made to develop more efficient electroactive materials that can detect biomarkers in wide range.

## Acknowledgements

We thank Prof. Yogesh Singh, Vice Chancellor Delhi Technological University, Delhi (India) for providing the research facilities. Suveen, Ashish, Saurabh and Shine are thankful to DTU, AICTE, DST and UGC for financial assistance, respectively.

## Appendix A. Supporting information

Supplementary data associated with this article can be found in the online version at http://dx.doi.org/10.1016/j.bios.2017.11.004.

## References

Ali, M.A., Singh, C., Mondal, K., Srivastava, S., Sharma, A., Malhotra, B.D., 2016. Mesoporous few-layer graphene platform for affinity biosensing application. ACS Appl. Mater. Interfaces 8 (12), 7646–7656.

Chen, Y.W., Liu, M., Kaneko, T., McIntyre, P.C., 2010. Atomic layer deposited hafnium oxide gate dielectrics for charge-based biosensors. Electrochem. Solid-State Lett. 13 (3), G29–G32.

Cheng, Y.-S.L., Rees, T., Wright, J., 2014. A review of research on salivary biomarkers for oral cancer detection. Clin. Transl. Med. 3 (1), 1.

Das, M., Dhand, C., Sumana, G., Srivastava, A., Nagarajan, R., Nain, L., Iwamoto, M., Manaka, T., Malhotra, B., 2011. Electrophoretic fabrication of chitosan− zirconium-oxide nanobiocomposite platform for nucleic acid detection. Biomacromolecules 12 (3), 540–547.

de Almeida, P.D.V., Gregio, A., Machado, M., De Lima, A., Azevedo, L.R., 2008. Saliva composition and functions: a comprehensive review. J. Contemp. Dent. Pract. 9 (3), 72–80.

Eliziário, S., Cavalcante, L., Sczancoski, J., Pizani, P., Varela, J.A., Espinosa, J., Longo, E., 2009. Morphology and photoluminescence of HfO 2 obtained by microwave-hydrothermal. Nanoscale Res. Lett. 4 (11), 1371.

Fahrenkopf, N.M., Rice, P.Z., Bergkvist, M., Deskins, N.A., Cady, N.C., 2012. Immobilization mechanisms of deoxyribonucleic acid (DNA) to hafnium dioxide ($HfO_2$) surfaces for biosensing applications. ACS Appl. Mater. Interfaces 4 (10), 5360–5368.
Giannobile, W.V., Beikler, T., Kinney, J.S., Ramseier, C.A., Morel, T., Wong, D.T., 2009. Saliva as a diagnostic tool for periodontal disease: current state and future directions. Periodontology 50 (1), 52–64.
Hu, S., Arellano, M., Boontheung, P., Wang, J., Zhou, H., Jiang, J., Elashoff, D., Wei, R., Loo, J.A., Wong, D.T., 2008. Salivary proteomics for oral cancer biomarker discovery. Clin. Cancer Res. 14 (19), 6246–6252.
Ibrahim, I., Lim, H., Huang, N., Pandikumar, A., 2016. Cadmium sulphide-reduced graphene oxide-modified photoelectrode-based photoelectrochemical sensing platform for copper (II) ions. PLoS One 11 (5), e0154557.
Kumar, S., Kumar, S., Ali, M., Anand, P., Agrawal, V.V., John, R., Maji, S., Malhotra, B.D., 2013. Microfluidic-integrated biosensors: prospects for point-of-care diagnostics. Biotechnol. J. 8 (11), 1267–1279.
Kumar, S., Kumar, S., Tiwari, S., Augustine, S., Srivastava, S., Yadav, B.K., Malhotra, B.D., 2016a. Highly sensitive protein functionalized nanostructured hafnium oxide based biosensing platform for non-invasive oral cancer detection. Sens. Actuators B: Chem. 235, 1–10.
Kumar, S., Kumar, S., Tiwari, S., Srivastava, S., Srivastava, M., Yadav, B.K., Kumar, S., Tran, T.T., Dewan, A.K., Mulchandani, A., 2015. Biofunctionalized nanostructured zirconia for biomedical application: a smart approach for oral cancer detection. Adv. Sci. 2 (8).
Kumar, S., Sharma, J.G., Maji, S., Malhotra, B.D., 2016b. A biocompatible serine functionalized nanostructured zirconia based biosensing platform for non-invasive oral cancer detection. RSC Adv. 6 (80), 77037–77046.
Kumar, S., Sharma, J.G., Maji, S., Malhotra, B.D., 2016c. Nanostructured zirconia decorated reduced graphene oxide based efficient biosensing platform for non-invasive oral cancer detection. Biosens. Bioelectron. 78, 497–504.
Lee, E.J., Ribeiro, C., Longo, E., Leite, E.R., 2006. Growth kinetics of tin oxide nanocrystals in colloidal suspensions under hydrothermal conditions. Chem. Phys. 328 (1), 229–235.
Lee, M., Zine, N., Baraket, A., Zabala, M., Campabadal, F., Caruso, R., Trivella, M.G., Jaffrezic-Renault, N., Errachid, A., 2012. A novel biosensor based on hafnium oxide: application for early stage detection of human interleukin-10. Sens. Actuators B: Chem. 175, 201–207.
Lee, Y.-H., Wong, D.T., 2009. Saliva: an emerging biofluid for early detection of diseases. Am. J. Dent. 22 (4), 241.
Li, T., Yang, M., 2011. Electrochemical sensor utilizing ferrocene loaded porous polyelectrrolyte nanoparticles as label for the detection of protein biomarker IL-6. Sens. Actuator B-Chem. 158 (1), 361–365.
Luo, X., Morrin, A., Killard, A.J., Smyth, M.R., 2006. Application of nanoparticles in electrochemical sensors and biosensors. Electroanalysis 18 (4), 319–326.
Malhotra, B., Das, M., Solanki, P.R., 2012. Opportunities in nano-structured metal oxides based biosensors. J. Phys.: Conf. Ser. 012007 (IOP Publishing).
Malhotra, R., Patel, V., Vaque, J.P., Gutkind, J.S., Rusling, J.F., 2010. Ultrasensitive electrochemical immunosensor for oral cancer biomarker IL-6 using carbon nanotube forest elctrodes and mutilabel amplification. Anal. Chem. 82 (8), 3118–3123.
Malhotra, R., Urs, A.B., Chakravarti, A., Kumar, S., Gupta, V., Mahajan, B., 2016. Correlation of Cyfra 21-1 levels in saliva and serum with CK19 mRNA expression in oral squamous cell carcinoma. Tumor Biol. 1–9.
Markopoulos, A.K., Michailidou, E.Z., Tzimagiorgis, G., 2010. Salivary markers for oral cancer detection. Open Dent. J. 4 (1).
Park, N.J., Zhou, H., Elashoff, D., Henson, B.S., Kastratovic, D.A., Abemayor, E., Wong, D.T., 2009. Salivary microRNA: discovery, characterization, and clinical utility for oral cancer detection. Clin. Cancer Res. 15 (17), 5473–5477.
Pavia, D.L., Lampman, G.M., Kriz, G.S., Vyvyan, J.A., 2008. Introduction to Spectroscopy. Cengage Learning.
Rajkumar, K., Ramya, R., Nandhini, G., Rajashree, P., Ramesh Kumar, A., Nirmala Anandan, S., 2015. Salivary and serum level of CYFRA 21-1 in oral precancer and oral squamous cell carcinoma. Oral. Dis. 21 (1), 90–96.
Shim, J., Rivera, J.A., Bashir, R., 2013. Electron beam induced local crystallization of $HfO_2$ nanopores for biosensing applications. Nanoscale 5 (22), 10887–10893.
Shin, J.-H., Hong, S.-H., 2014. Fabrication and properties of reduced graphene oxide reinforced yttria-stabilized zirconia composite ceramics. J. Eur. Ceram. Soc. 34 (5), 1297–1302.
Solanki, P.R., Kaushik, A., Agrawal, V.V., Malhotra, B.D., 2011. Nanostructured metal oxide-based biosensors. NPG Asia Mater. 3 (1), 17–24.
Solanki, P.R., Kaushik, A., Chavhan, P., Maheshwari, S., Malhotra, B., 2009. Nanostructured zirconium oxide based genosensor for Escherichia coli detection. Electrochem. Commun. 11 (12), 2272–2277.
Srivastava, S., Kumar, V., Ali, M.A., Solanki, P.R., Srivastava, A., Sumana, G., Saxena, P.S., Joshi, A.G., Malhotra, B., 2013. Electrophoretically deposited reduced graphene oxide platform for food toxin detection. Nanoscale 5 (7), 3043–3051.
Teymourian, H., Salimi, A., Firoozi, S., Korani, A., Soltanian, S., 2014. One-pot hydrothermal synthesis of zirconium dioxide nanoparticles decorated reduced graphene oxide composite as high performance electrochemical sensing and biosensing platform. Electrochim. Acta 143, 196–206.
Teymourian, H., Salimi, A., Khezrian, S., 2013. $Fe_3O_4$ magnetic nanoparticles/reduced graphene oxide nanosheets as a novel electrochemical and bioeletrochemical sensing platform. Biosens. Bioelectron. 49, 1–8.
Tiwari, S., Gupta, P.K., Bagbi, Y., Sarkar, T., Solanki, P.R., 2016. L-cysteine capped lanthanum hydroxide nanostructures for non-invasive detection of oral cancer biomarker. Biosens. Bioelectron.
Vasudev, A., Kaushik, A., Bhansali, S., 2013. Electrochemical immunosensor for label free epidermal growth factor receptor (EGFR) detection. Biosens. Bioelectron. 39 (1), 300–305.
Wang, Z., Zhang, J., Guo, Y., Wu, X.Y., Yang, W., Xu, L., Chen, J., Fu, F., 2013. A novel electrically magnetic controllable eectrochemical biosensor for the ultrasensitive and specific detection of attomolar level oral cancer-related microRNA. Biosens. Bioelectron. 45, 108–113.
Xie, J., Cao, H., Jiang, H., Chen, Y., Shi, W., Zheng, H., Huang, Y., 2013. $Co_3O_4$-reduced graphene oxide nanocomposite as an effective peroxidase mimetic and its application in visual biosensing of glucose. Anal. Chim. Acta 796, 92–100.
Xu, F., Deng, M., Li, G., Chen, S., Wang, L., 2013. Electrochemical behavior of cuprous oxide–reduced graphene oxide nanocomposites and their application in nonenzymatic hydrogen peroxide sensing. Electrochim. Acta 88, 59–65.
Yang, Y., Liu, Q., Liu, X.-P., Liu, P.-Z., Mao, C.-J., Niu, H.-L., Jin, B.-K., Zhang, S.-Y., 2016. Multifunctional Reduced Graphene Oxide (RGO)/Fe 3 O 4/CdSe Nanocomposite for Electrochemiluminescence Immunosensor. Electrochim. Acta 190, 948–955.